

Geologic Storage of CO₂

Subsurface Monitoring of CO₂ Storage in Coal

*GCEP Annual Report
April, 2009*

Investigators

Jerry M. Harris, Professor, Geophysics

Youli Quan, Research Associate, Geophysics

Jolene Robin-McCaskill, Adeyemi Arogunmati, Evan S. Um, Tieyuan Zhu

Graduate Research Assistants, Geophysics

Abstract

True 4-D seismic subsurface monitoring for CO₂ storage in Coal is examined. Our GCEP project is divided into two tasks: (1) Innovative scenarios for continuous seismic monitoring, and (2) development of a laboratory measurement for the signature of CO₂ in coal. Under task #1, we have carried out a comprehensive simulation study that involved reservoir simulation, seismic simulation, and simulated depth imaging. The goal was to test and demonstrate the efficacy of True 4-D subsurface monitoring. The approach we take may be succinctly described as trading off spatial resolution for higher temporal resolution. The fourth-dimension in True 4-D monitoring is the dense sampling of slow time. With the help of this slow time axis we have developed a methodology for early detection of leaks or small changes in a reservoir due to CO₂. We propose to use permanently embedded data acquisition hardware, and dynamic imaging. Dynamic imaging is implemented through either iterative inversion of continuously streaming data or evolution of sparse datasets. We also summarize the development of a finite element method for simulating transient electromagnetics for subsurface monitoring, especially for a relatively shallow target like coal. The algorithm is especially well suited for complex geology and surface tomography.

The True 4-D monitoring task is complemented by a laboratory activity on the acoustic signature of CO₂ in coals. In particular, this task seeks to add pressure control to DARS I and measure the acoustic compressibility and attenuation of saturated coal at approximately 1000 Hz.

Table of Contents

Investigators

Abstract

1. True 4-D Subsurface Monitoring

- *Flow Simulation of CO₂ Sequestration in Coalbed*
- *Simulated Seismic Depth Imaging*
- *The Case of Full 3-D Surveys*
- *The Case of Sparse 3-D Surveys*
- *Embedded data acquisition and Pre-stack Data Approach*
- *Dynamic Inversion for Qualitative Interpretation*

2. An Approach to Quasi-continuous Time-lapse Seismic Monitoring with Sparse Data

- *Introduction*
- *Theory*
- *Time-lapse Field Monitoring Example*
- *Time-lapse Synthetic Monitoring Example*
- *Summary – True 4-D Monitoring*

3. Estimating the Attenuation of Porous Rock with Changing Pressure and Saturation using DARS

- *DARS II Construction*
- *DARS Numerical Simulation*

4. A Finite Element Algorithm for 3D Transient Electromagnetic Modeling

- *Theory and Method*
- *Time-domain CSEM Simulation Examples*
- *Conclusions – Electromagnetic Simulations*

Future Work

Publications

References

Contacts

1. True 4-D Seismic Subsurface Monitoring

Traditional 4-D seismic subsurface monitoring uses multiple 3-D seismic snapshots to capture temporal changes of the reservoir. The snapshots are repeatedly acquired at time intervals of several months to years. In our approach, reservoir time or “slow” time is the independent fourth dimension. We propose to sample slow time quasi continuously, thus the name True 4-D. The traditional approach suffers from serious temporal aliasing. More importantly, while sensitive to reservoir changes due to CO₂ it may fail to detect a dangerous leak in a geological storage site for months of years because of inadequate temporal sampling. Figure 1 illustrates the traditional snapshot approach. It can be seen that we have difficulty to identify a small leak (circled) from a single snap shot, especially in the present of noise. However, if we have quasi-continuous data in the temporal axis as shown in Figure 2, the leak or other temporal changes can be easily identified with the help of the true time axis. As shown in Figure 3, we expect quasi-continuous monitoring to detect the leak sooner.

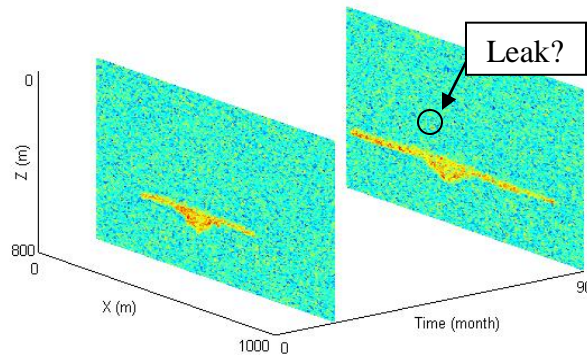


Figure 1: Traditional monitoring uses a large temporal sampling interval. The images are 2-D seismic profiles corresponding to two discrete observation times. It is difficult to identify a leak (circled) from these two images.

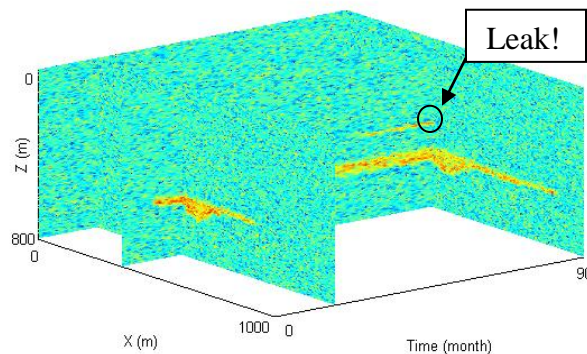


Figure 2: Monitoring with a small (True 4-D or quasi-continuous) temporal sampling interval. When we have a large number of time-lapse images, we can better separate signal from noise, in this case the small leak from spatially noisy image.

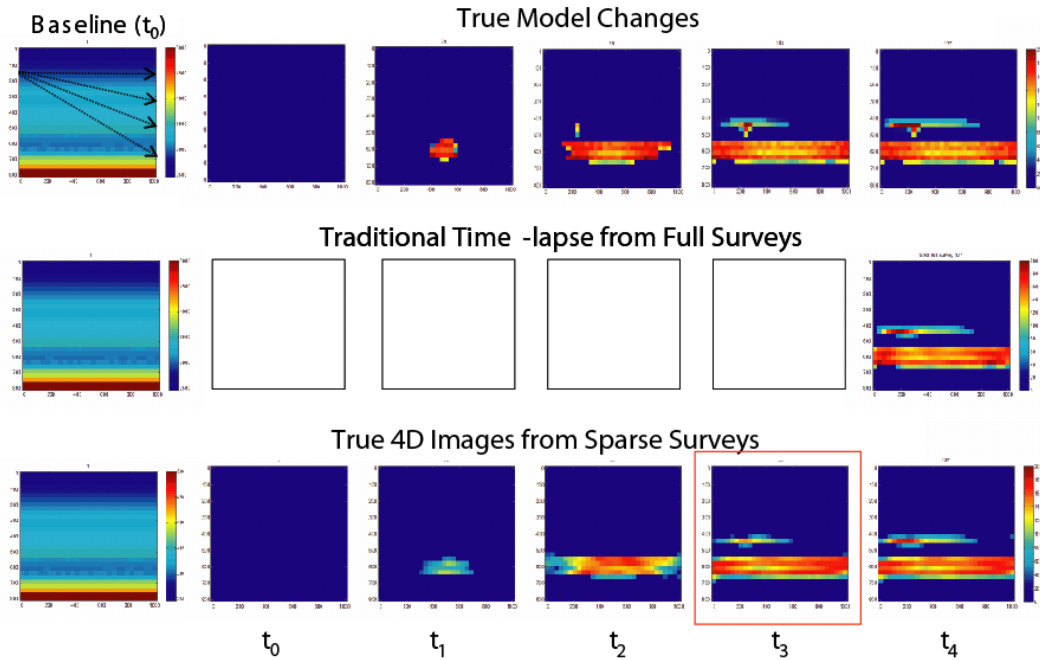


Figure 3: Quasi-continuous monitoring can detect a leak earlier as indicated at time t_3 .

In this report we describe a series of synthetic tests to investigate the feasibility of True 4-D. True 4-D approach can overcome the temporal aliasing problem and help interpret subtle temporal changes. However, the cost of true 4-D monitoring will be prohibitively high if we just simply reduce the time interval between surveys and repeatedly collect complete data as done in the traditional approach. We assume the running costs of True 4-D should be comparable to the traditional approach, though spread over time and with some higher startup expense for embedded instrumentation. To accomplish this, we trade spatial resolution for temporal resolution, use embedded data acquisition systems, dynamic imaging, and/or sparse data evolution algorithms to implement True 4-D monitoring.

In following subsections, a comprehensive synthetic study of True 4-D seismic monitoring is reported. We construct a 3-D coalbed model, run a flow simulator to simulate CO₂ storage, and use simulated seismic depth imaging and finite difference seismic modeling to study the various data acquisition and processing strategies that have the potential of making True 4-D practical. In a separate section, sparse data evolution technique is discussed.

Flow Simulation of CO₂ Storage in a Coalbed

An illustrative geological model for a 3-D coalbed was built with GOCAD based on the work of Ross (2007). The model, consisting of three layers (coal, shale and sand), is shown in Figure 4. The model is imported into flow simulator GEM (www.cmgroup.com)

for the simulation for CO₂ injection and storage. The simulated flow models are output in time steps of weeks and months for 8 years.

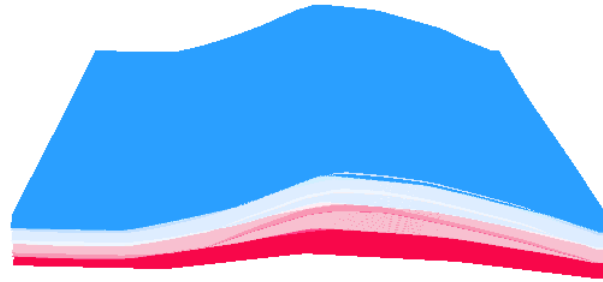


Figure 4: The coalbed model used in this monitoring study. The size of the model is about 1000 x 900 x 50 (m³), and the depth is about 500 m. From top to bottom, the three layers are sand, shale, and coal. Here, the overlying shale serves as reservoir seal. We put a low permeability hole in this shale layer to simulate a leakage into the overburden.

Initially the model is water saturated. We assume injection begins on January 1, 2008. As CO₂ is injected into the coalbed, a volume becomes gas saturated. Figure 5 shows the gas saturation in the coal layer at four different times. The shale layer above the coal normally maintains a seal that keeps the injected CO₂ within the coal. To mimic a possible leakage, we place a high permeability channel in the shale. Figure 6 shows the gas saturation at two times as leaking through the seal begins and spreads in the top sand layer.

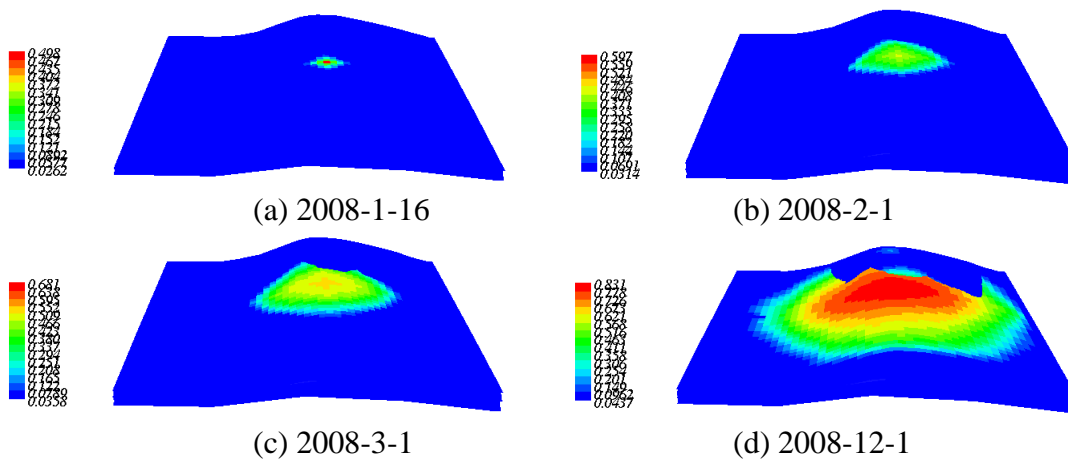


Figure 5: Gas saturation changes within coalbed. The objective of subsurface monitoring is to track the gas front and detect possible leakage into the overburden.

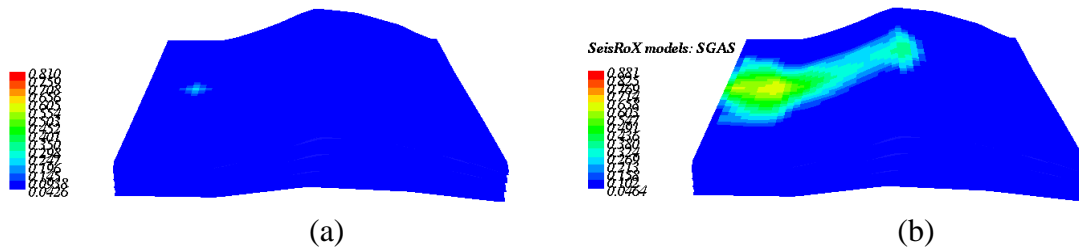


Figure 6: CO₂ leaking occurs through a high permeability channel and spreading in the sand layer above: (a) 9-1-1009. CO₂ leaks begins; (b) 10-1-2010. Leak spreads in overburden sand.

Simulated Seismic Depth Imaging

The time-lapse flow models (including porosity, permeability, water saturation, gas/CO₂ saturation and pore pressure) are imported into simulated seismic depth imaging software SeisRox (www.norsar.com) for the monitoring study. Simulated seismic depth imaging convolves the reflectivity model with illumination vectors. This method of simulating depth migration is preferred over 1-D wavelet convolution because it includes the effects of acquisition geometry, 3-D illumination, ray paths, anisotropy and lateral resolution in complex models (Lecomte & Kaschwich, 2008). With SeisRox we can convert flow snapshots into seismic velocity snapshots and compute simulated 3-D depth images without the compute intensive shot simulation and migration steps. Figure 7 shows the initial velocity model, converted from the initial flow model. Figure 8 shows the velocity changes about one year later, 10-1-2009. The traditional approach is to calculate 3-D seismic data using the finite difference method, and then perform depth imaging. It may take days to get forward modeling and migration imaging done for a single 3-D model. Now we have more than one hundred time-lapse models, and it is impossible to do this in the conventional way. The simulated seismic depth imaging, however, is very fast. It takes a few hours to computer hundreds of 3-D depth images. In order to compute the seismic images, 1-D overburden layers are added to the top o the reservoir. Next we will use simulated depth imaging to demonstrate the concepts of true 4-D monitoring and study the strategies for true 4-D monitoring.

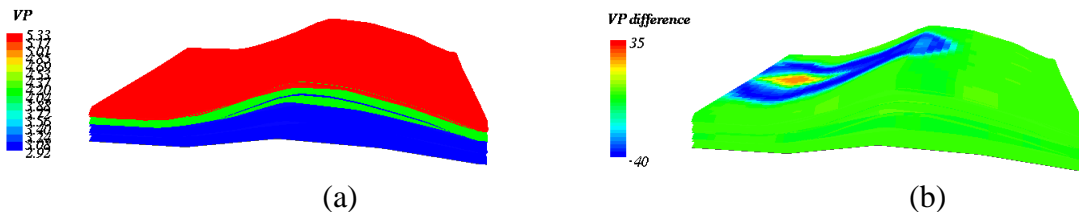


Figure 7: Velocity models converted from flow models. The velocity change shown in (b) is the difference between the initial model and the model approximately one year later.

The Case of Full 3-D Surveys

When a site is first selected as a potential candidate for CO₂ storage, a detailed site characterization must be performed. The first baseline characterization must include a full coverage 3-D survey with state-of-the-art-technology. Figure 8 shows the traditional data acquisition geometry, with the model and imaging target used in our simulation. Figure 9 is the depth image differences between given times and the initial time.

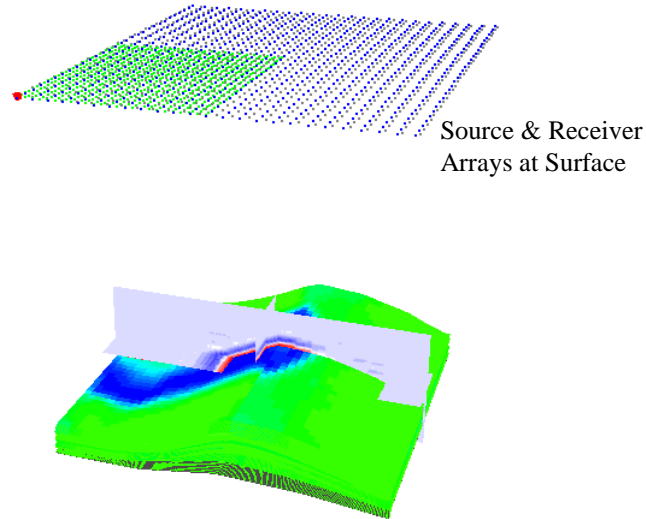


Figure 8: A full 3-D data acquisition geometry. Green dots are the mid-points corresponding to the source (red dot). Blue dots indicate receiver locations. Gray dots are source arrays. Three planes in the model show slices through the depth images at the target area.

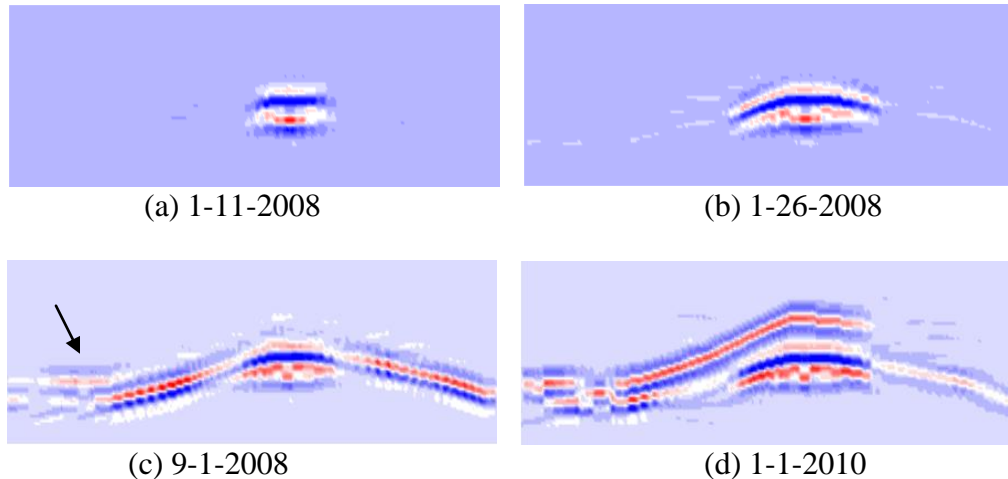


Figure 9: Depth image differences at four different times. The subsurface image at a given time is subtracted from the image corresponding to the baseline model. The leak starts around 9-1-2008.

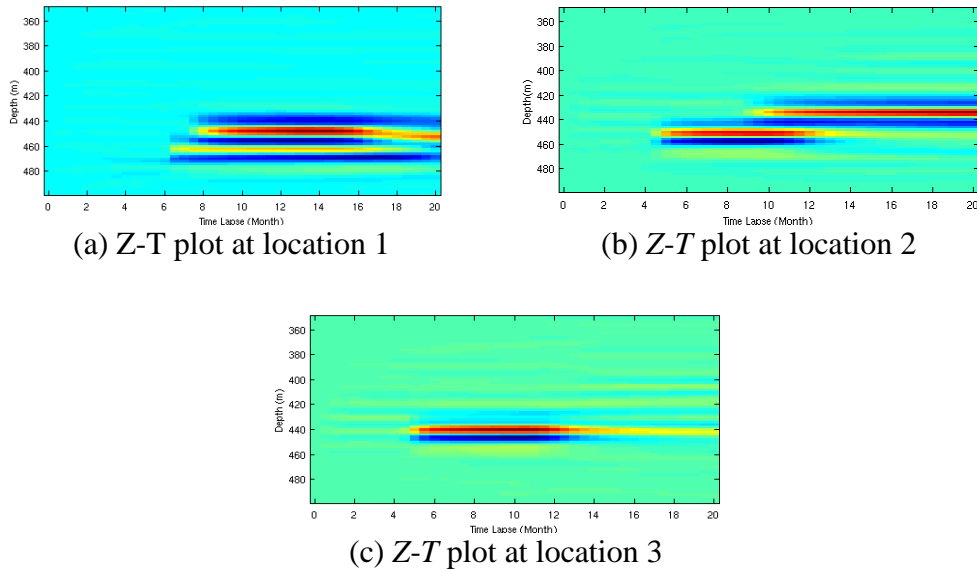


Figure 10: 2-D visualization of continuous monitoring data. A profile at a specified surface location is displayed versus slow-time. The resulting plot is a depth vs. slow-time display.

Quasi-continuous monitoring creates a huge volume of data, e.g., Data (X, Y, Z, T) . We can visualize subsets of the True 4-D dataset in many different ways. A particularly revealing 2-D image is to select a (X, Y) surface location and display the (Z, T) plane as shown in Figure 10. There are two features in Figures 10a and 10b. The upper one is the leakage of CO_2 in the sand layer and lower one is CO_2 storage in the coal. Since these two images come from different (X, Y) locations, we can see the CO_2 reaches the locations them at different times. The two events begin at location 1 at almost the same time. This is because location 1 is very close to the leaking channel. Location 3 is far away from the leaking channel, and only one event appears. The example in Figure 10 tells us that a small change in subsurface conditions has a very good chance to be seen with the help of the new slow-time axis.

The Case of Sparse 3-D Surveys

The acquisition of a full 3-D seismic survey is very expensive and requires a long period of time. It is impractical to do True 4-D monitoring with regular full surveys. We now present another extreme case of 3-D acquisition geometry as shown in Figure 11, which consists of a source array and a receiver array. This simple cross array geometry generates a true 3-D image albeit at single fold (Harris et al. 2006; Walton 1972). However, it may not produce adequate signal-to-noise because of its low fold. We here use simulated depth imaging as an idealized seismic migration to see how it works. Figure 12 is the depth difference image obtained from cross array geometry. Clearly, the migration artifacts are severe, though the effects of CO_2 injection can also be seen.

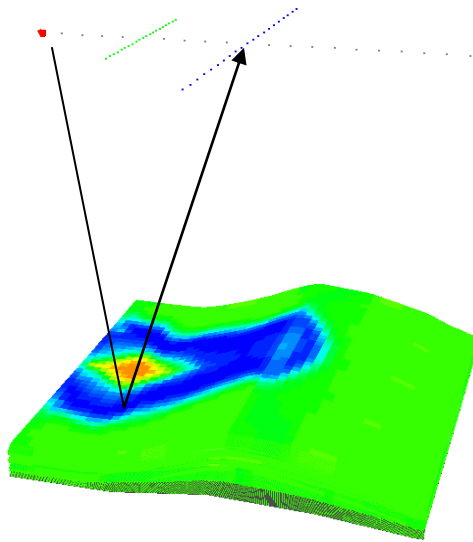


Figure 11: Cross array acquisition geometry that has a source array (gray dots) and receiver array (blue dots). The green dots show the mid-points for the given source (red square).

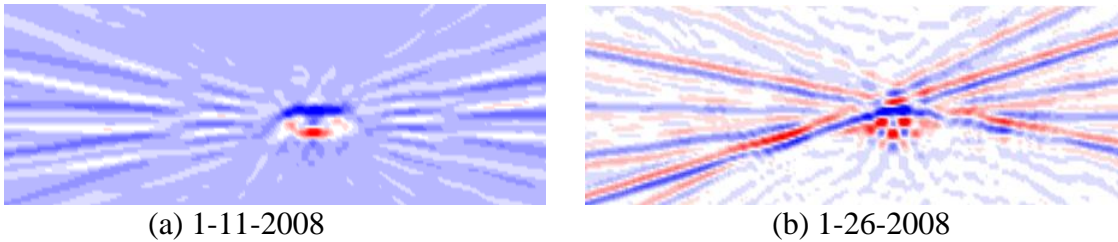


Figure 12: Depth difference images (relative to baseline). It can be seen that the imaging artifacts are dominant.

Embedded Source and Receiver and Pre-stack Data Approach

We have discussed the two extreme cases (full survey and the sparse cross-array survey) in the previous subsections. The cost and quality are the main problems for continuous monitoring. It seems we need to choose a proper trade-off between them. The migration-based imaging approach usually requires dense data acquisition geometry that is quite difficult if we want to carry out continuous monitoring. This motivates us to use pre-stack data directly.

We propose to embed sources and receivers (Figure 13a) near the surface and continuously collect the data, say every week. Then the recorded trace can be display in a plot of seismic time (fast) and reservoir time (slow). To test this idea, we use the finite

difference method and the time-lapse velocity models to compute the seismic data. The computed seismic traces are displayed in Figure 13b. The attribute is amplitude difference. The horizontal axis shows the time when the data is collected. The travel-time and amplitude of the seismic reflection change slightly as CO₂ injection continues.

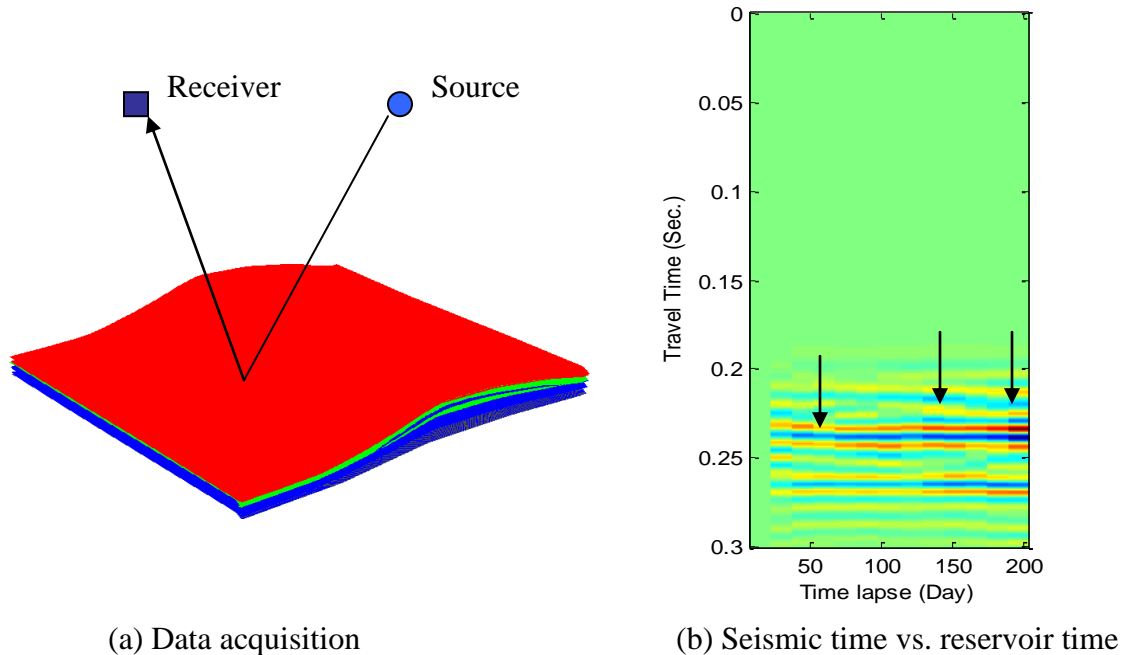


Figure 13: Embedded sources and receivers for continuous operation and the corresponding time image reflect the subsurface changes.

Dynamic Inversion for Quantitative Interpretation

Although we can see the changes in the raw seismic data, it will be very helpful if we perform seismic inversion and transform the amplitude vs. time data into acoustic impedance or other elastic properties of subsurface vs. depth. The True 4-D seismic monitoring is a typical dynamic process. The dynamic inversion approaches introduced by Quan & Harris (2008) and Jin et al. (2008) are especially suitable for our continuous data. We are currently working on the dynamic inversion for the data shown in Figure 13b. After the dynamic inversion finished, we will have a ($Z-T$) image with the elastic attributes.

In addition to the methods discussed in this section, we are also working on another method for quasi-continuous seismic monitoring which will be presented in the next section.

2. An Approach to Quasi-continuous Time-lapse Seismic Monitoring using Data Evolution of Sparse Data Recording

We take the advantage of small changes in the seismic property of a geological reservoir that are expected to occur in a small time interval. The goal of this approach is to obtain high temporal and spatial resolution in reconstructed, time-lapse geophysical images using comparable resources that would have provided high spatial but low temporal resolution images with conventional approaches. This is done by acquiring spatially sparse data at small time intervals. In this case, a spatially sparse dataset refers to that dataset which is a small fraction (as little as 5%) of what would be acquired to reconstruct a high spatial resolution tomographic image of the subsurface. The high spatial resolution obtained by the proposed approach occurs because unrecorded data are predicted from future and past data. With high temporal and spatial resolution, early detection of important reservoir changes is more likely to occur.

Introduction

Geophysical imaging has played a large part in subsurface monitoring projects, especially in petroleum reservoir monitoring projects (e.g., Harris et al., 1995; Rickett and Lumley, 2001). This is primarily due to the kind of seismic changes that occur in the reservoir rock properties (Wynn, 2003). In addition, seismic data analysis is a well developed and understood subject (Yilmaz, 1987; Yilmaz, 2001). Seismic signals are able to penetrate deep into the earth and can be used in virtually any geologic setting (Wynn, 2003). The use of seismic tomography in time-lapse monitoring takes advantage of the changes in a seismic property of the reservoir rock during the time interval under consideration. For example, a reservoir velocity model can be quantitatively reconstructed from either seismic reflection or transmission traveltimes using tomography.

Consider a time-lapse seismic monitoring study designed to last for several decades as might be the case in whole-life monitoring of a petroleum reservoir or for a CO₂ storage site. The conventional approach is to acquire a large amount of seismic data such that a high spatial resolution image of the subsurface can be obtained each time a dataset is acquired. The time intervals between successive data acquisition campaigns are often so large that there are large changes in the successive seismic data acquired. The time intervals are usually of the order of years (e.g., Mathisen et al., 1995; Landrø et al., 1999; Arts et al., 2004). Such a strategy works very well for some time-lapse projects but for other applications such as monitoring CO₂ storage, the late identification of a reservoir leak by a year could have dire consequences. In other words, some time-lapse monitoring strategies are more effective when the changes in successive time-lapse datasets are small. In such cases, temporal resolution is as important as spatial resolution, and sometimes, more important.

If resources are to be kept comparable, two scenarios are possible – acquiring data such that the monitoring provides either high spatial resolution and low temporal resolution images, or low spatial resolution and high temporal resolution. In the second scenario, low spatial resolution results because a small amount of data is acquired each time, and

high temporal resolution results because data are acquired more frequently. The traditional approach to inverting sparse data is to reduce the number of model parameters solved. Because only a fraction of the data that will normally be used to get a high resolution image is used, the resulting seismic image has a lower spatial resolution. We propose to estimate unrecorded data (Harris et al., 2004; 2007; 2008), and then reconstruct geophysical models without reducing the number of model parameters solved, thereby maintaining the high spatial resolution.

Although the idea posed here is somewhat similar to the recently developed concept of compressive sampling (Candès and Romberg, 2007) in the sense that sparse data are acquired and used in estimating unrecorded data, we deal here with datasets that are even sparser than what would be acquired as compressive sampling. Also, we take advantage of the large portion of the data space available in the dense baseline data.

Theory

Let the dense time-lapse data be composed of a recorded sparse part and an unrecorded part. i.e.

$$\mathbf{d}_d = \mathbf{S}\mathbf{d}_d + (\mathbf{I} - \mathbf{S}) \mathbf{d}_d \quad (1)$$

$$\mathbf{d}_d = \mathbf{d}_s + \mathbf{d}_u \quad (2)$$

where \mathbf{S} is the data sampling operator that selects which data are recorded from the “dense” dataset \mathbf{d}_d , and \mathbf{d}_s and \mathbf{d}_u are “sparse” and “unrecorded” datasets respectively. From (1) and (2), we see that

$$\mathbf{d}_s = \mathbf{S}\mathbf{d}_d, \quad \mathbf{d}_u = (\mathbf{I} - \mathbf{S}) \mathbf{d}_d \quad (3)$$

In this notation, each vector \mathbf{a} contains all previously measured and some future measured data. Our goal is to find an estimate $\tilde{\mathbf{a}}_u$ for the unrecorded dataset from the measured data \mathbf{a}_s . The fitting goal for estimating finding $\tilde{\mathbf{a}}_u$ is

$$\mathbf{A}\mathbf{d}_d \approx \mathbf{0} \quad (4)$$

subject to the constraint

$$\mathbf{d}_s = \mathbf{S}\tilde{\mathbf{d}}_d \quad (5)$$

where in (4) the operator \mathbf{A} is the model constraint or estimation operator. Substitution of (2) into (4) gives

$$\mathbf{A}\mathbf{d}_s + \mathbf{A}\tilde{\mathbf{d}}_u \approx \mathbf{0} \quad (6)$$

The estimated unrecorded data, \tilde{d}_u is then obtained using (6), and minimizing the objective function

$$\Phi = \left\| \mathbf{A} \tilde{d}_u + \mathbf{A} d_s \right\|^2 \quad (7)$$

Time-lapse Field Monitoring Example

The field data example presented here are crosswell data from the McElroy field in West Texas. The datasets were acquired to monitor velocity changes in the reservoir in response to CO₂ injection (Harris et al., 1995; Lazaratos and Marion, 1997) between 1993 and 1995. The wells are over 3000ft deep and are separated by approximately 600ft. Figure 14 shows common-shot gathers data from the surveys. First arrival seismic traveltimes were picked from the data. The largest traveltimes differences occur at the depths corresponding to the location of the reservoir between 2750 and 3150 ft. Using these traveltimes, velocity models were reconstructed using the tomography code, FAST (Zelt and Barton, 1998). Figure 15 shows the reconstructed velocity models and the difference between them when the complete dataset in both cases are used. The most obvious difference in the velocity models is the significant drop in the p-wave velocity between 1993 and 1995, resulting from the injection of CO₂ into the reservoir.

Having a time interval of two years between the baseline image and the monitor image is satisfactory for some monitoring projects. However, if potentially dangerous consequences could occur from an abnormality in the reservoir, it will be necessary to monitor the reservoir with a finer sampling in time. Also, if resources necessary for data acquisition are limited, a more efficient time-lapse monitoring strategy is needed. This, scenario illustrates the need for a quasi-continuous monitoring strategy using sparse data.

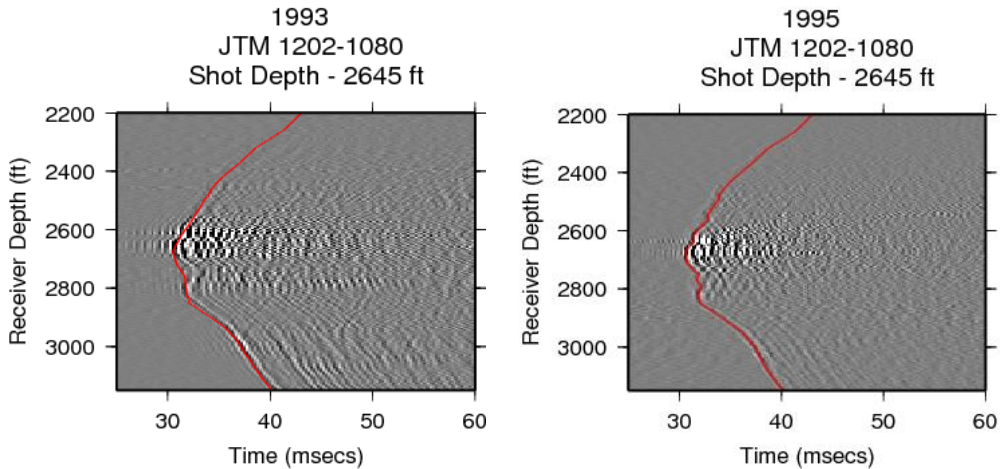


Figure 14: Common-source gathers from the 1993 and the 1995 surveys at the McElroy field in West Texas. The red lines indicated first arrivals.

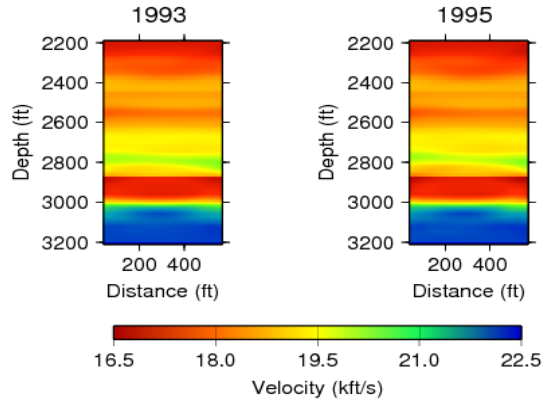


Figure 15: Reconstructed velocity models from the baseline (1993) and monitor (1995) surveys, and the difference between both models.

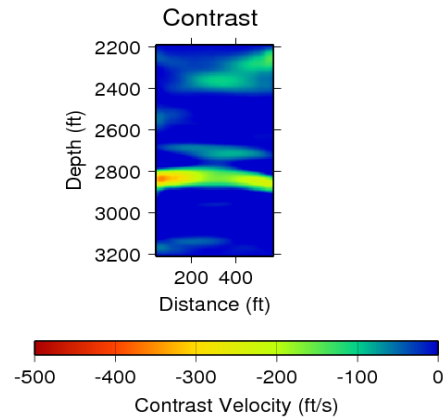


Figure 16: Reconstructed contrast model from the decimated 1995 field dataset.

To test the efficiency of the approach presented in this paper on field data, we used the complete dataset from the 1993 survey and 1% of the dataset from the 1995 survey to estimate the discarded data from the 1995 dataset. Here, the \mathbf{A} operator in equation (7) was the first order derivative. The velocity models were then reconstructed from the estimated data. Figure 16 shows the resulting contrast model. We obtained a good comparison between the true contrast model and the contrast model from the reconstructed dataset.

Time-lapse Synthetic Monitoring Example

In order to test this approach of quasi-continuous monitoring, we created a series of 70 two-dimensional P -wave velocity models from the baseline model reconstructed using the 1993 dataset, and a set of simulated fluid flow models converted to velocity models. The conversion was done using a Gassmann fluid substitution model. These models are intended to simulate CO_2 injection into the reservoir over a period of 32 months. We included a fracture in the model which allowed injected CO_2 to flow out of the reservoir.

Leakage occurred after the injected CO₂ reached the fracture zone approximately 10 months after the start of injection.

Using the finite differencing eikonal solver scheme given by Hole and Zelt (1995), we calculated dense first arrival seismic traveltimes recorded in a crosswell data acquisition geometry for all 70 synthetic velocity models. Gaussian noise with a standard deviation that we consider to be the picking error of the field data was then added to the synthetic dataset. To simulate sparse data, we reduced the data size to 10%, 5%, 2%, and 1% of the original size for a given dataset in time. The reduction was done such that the total data volume in each sampling scenario was constant. From these sparse synthesized datasets, we estimated the dense datasets using the methods described in the previous section, and then reconstructed the corresponding velocity models using traveltime tomography.

In estimating missing data, we used zeroth, first and second order derivative operators as the **A** operator in equation (7). We then used the resulting dataset to reconstruct the synthetic velocity models. We present the results of the reconstructed velocity models by their root mean square (rms) errors with respect to the known synthetic models (Figure 17). In this case, we use the rms errors measured in the regions of the model where changes are known to occur. The rms error curves of the estimated datasets show a consistent pattern. This implies that we can maintain an approximately equal level of misfit in our estimated datasets and reconstructed velocity models if we reduce data size and sample the data space more frequently in time. From the plots, we see that the rms error reduces with time, indicating the impact of additional data on data estimation. What is not captured by the rms error plots is that using only 1% data measured every two weeks, the leaked CO₂ was detected soon after it occurred. With the conventional strategy such a leak might not be discovered for years.

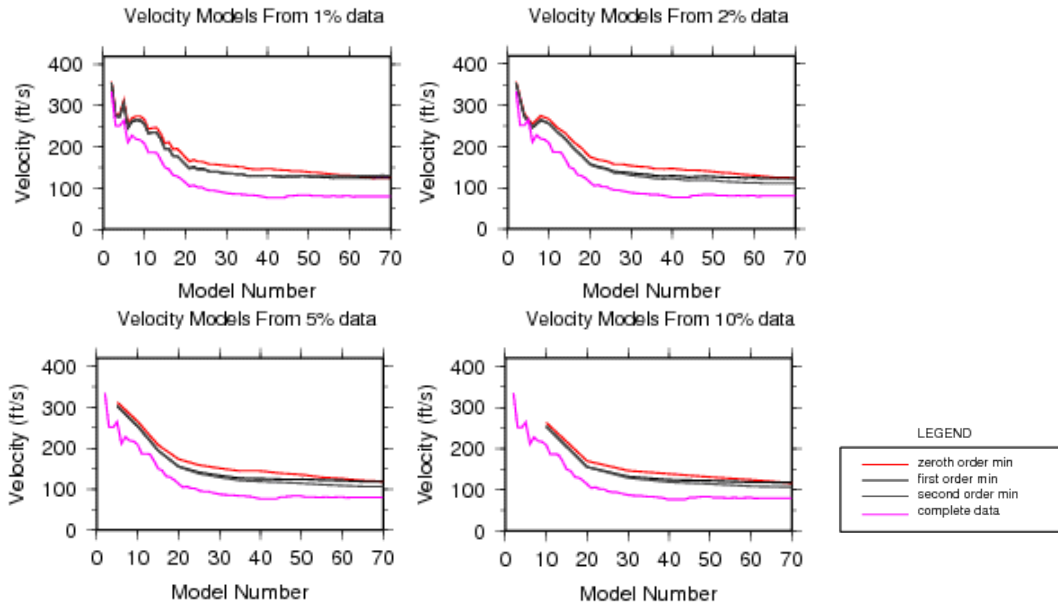


Figure 17: RMS error plots of the reconstructed velocity models using the estimated datasets.

Summary – True 4D and Data Evolution

We have presented monitoring methodologies for True 4-D seismic monitoring of CO₂ storage. First, we simulated surface acquisition scenarios of full and sparse surface arrays with simulated depth migration. Then we showed how data evolution can be used to fill in missing data before processing. Data evolution proved quite effective for both synthetic and field datasets. In the synthetic example, the CO₂ leak which occurred in the synthetic reservoir was detected early. Even though we assumed crosswell seismic acquisition geometry, data evolution can be applied to data acquired using any kind of data acquisition geometry. We intend to continue research in the area of time-lapse seismic monitoring with sparse seismic data using full seismic traces. Future work will involve the development of techniques that will take advantage of time dependent data covariance in time-lapse data. The most challenging aspect of data evolution is deciding on the optimal data size that produces the desired results, and the optimal time-lapse survey design. The benefit of data evolution is the ability to sample the data space more frequently in time with much less data without significantly losing spatial resolution in reconstructed velocity models. Also temporal resolution is increased with increased temporal sampling.

3. Estimating the Attenuation of Porous Rock with Changing Pressure and Saturation using Differential Acoustic Resonance Spectroscopy (DARS)

The objective of this work is to measure the acoustic compressibility and attenuation of coal under varying pressure and saturation. This laboratory measurement can provide useful information for seismic subsurface monitoring in CO₂ saturated coals. The previous DARS I system does not have pressure capability.

DAR II Construction

The first generation of DARS, called DARS I, measures the acoustic compressibility and attenuation at atmosphere pressure and conditions of full saturation. A cross section of DARS I is shown in Figure 1 and its signal path is shown in Figure 2. The SR850 lock-in amplifier generates the signal that is sent to the BNC3090 power amplifier that drives the PZT source. The PZT source excites the sound waves in the fluid, e.g., silicone oil. The hydrophone detects the signal and sends it to a B&K2635 charge amplifier, which amplifies the signal and returns it to the SR850 lock-in amplifier for phase locked measurement of the amplitude versus frequency.

DARS II is designed to have independent control on pore pressure and saturation and confining pressure. The design for DARS II is to take the DARS I set up and place it into a pressure vessel. A picture of the DARS II system is shown in Figure 3. DARS II has a high-capacity pressure pump connected to the pressure vessel. Inside the pressure vessel is an aluminum cavity which is ~18 inches in length with a piezoelectric disc source located at the bottom of the pressure vessel and a hydrophone receiver located at the top of the cavity for signal generation and detection.

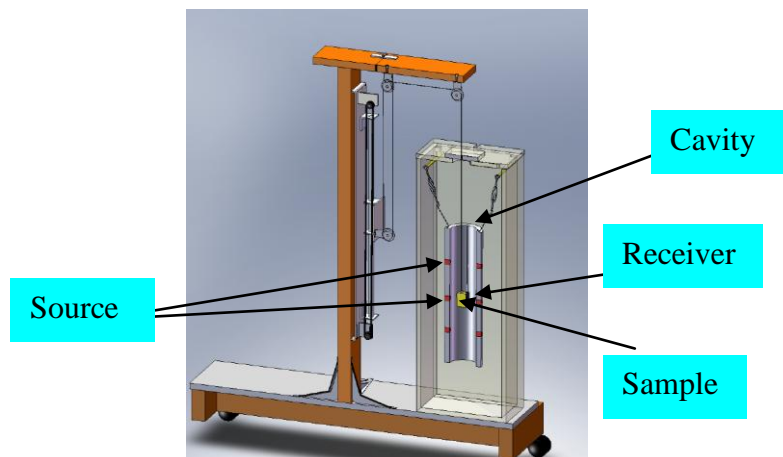


Figure 18: DARS I Cross Section

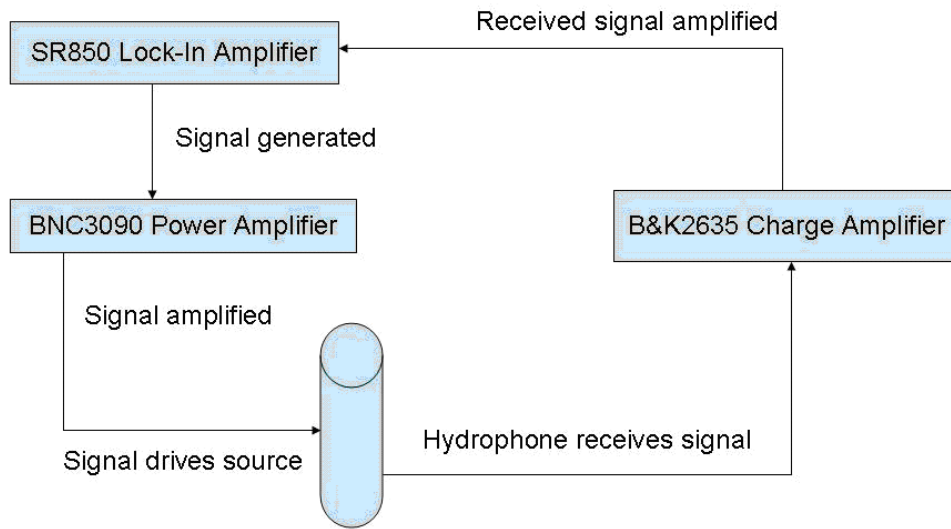


Figure 19: Signal path of DAR I

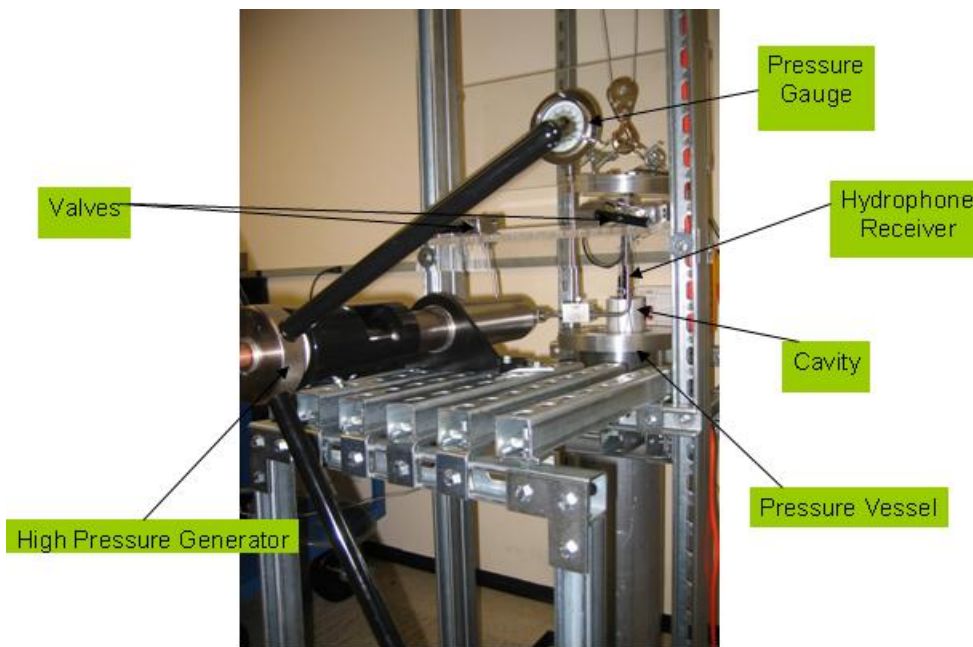


Figure 20: DAR S II pressure

The system Q for DAR S II is about 240 at atmosphere pressure. This is reduced from

DARS I, whose Q is about 300. The resonant frequency of the DARS I system is about 1080 Hz, whereas for DARS II the resonant frequency is about 750 Hz. The cavity has been increased in length by about 2 1/2 inches and thus the decrease in resonant frequency. The drop in Q from DARS I to DARS II was not expected. From Figure 5, one can see that the drop in Q is due changes in both resonance frequency and linewidth. More measurements and analysis will be performed to better understand this change in Q .

Preliminary measurements were made using the DARS II system at different pressures. First the pressure vessel is filled with silicone oil. The system is vacuumed for about 5 minutes, then measurements were taken at 0, 50, 100, 150 and 200 psi, respectively. The results are shown in Figures 4-5.

Two accomplishments in DARS II development have been made. One accomplishment is determining the best source and receiver configuration for the DARS II pressure conditions. The second accomplishment is placing pressure on the DARS II system and taking measurements with the empty system. All the confining pressure component components work as they should, however, we must fix some leaks in order to go to higher confining pressures. We plan to conduct set of samples measurements under various pressures. Also, the pore pressure portion of DARS II needs to be added; parts for the latter have been designed and some ordered.

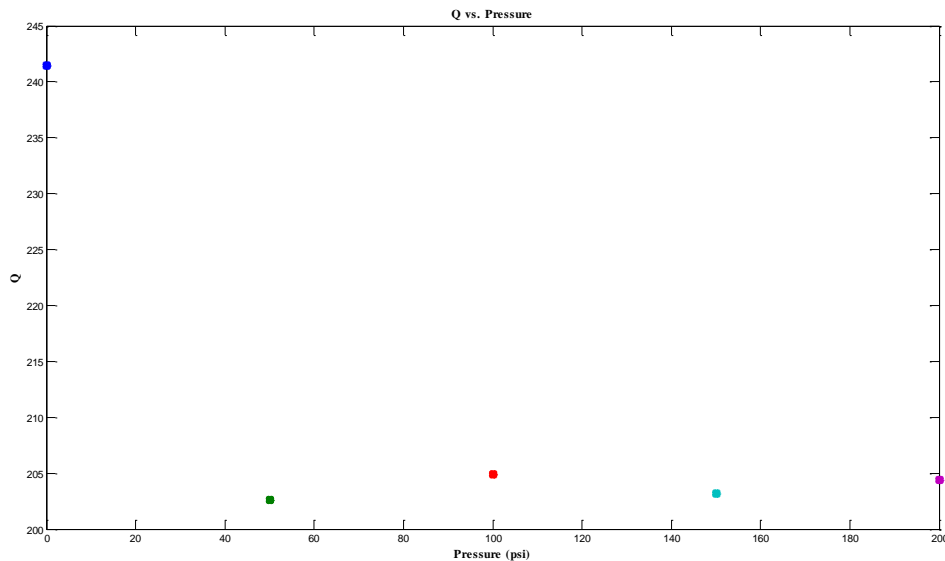


Figure 21: DARS II Q vs. Pressure.

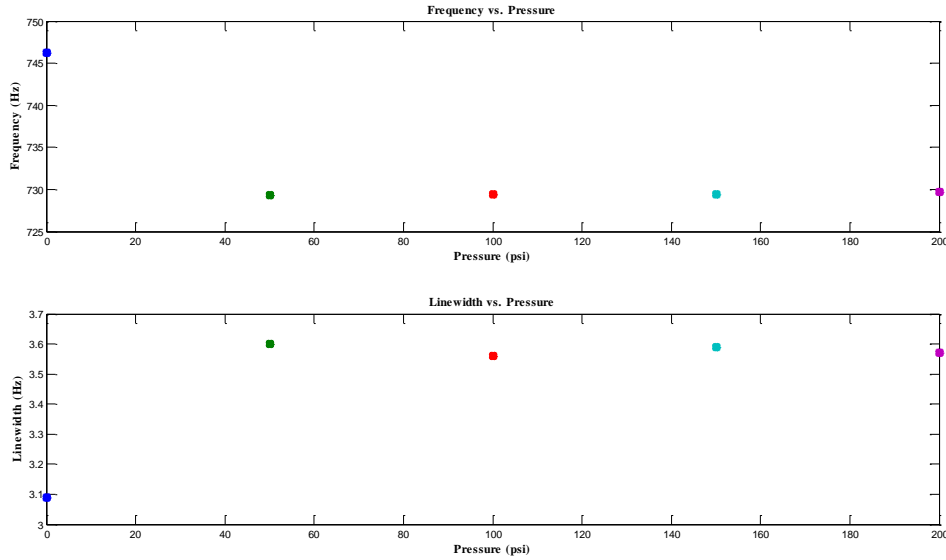


Figure 22: DARS II Resonant Frequency and Linewidth vs. Pressure.

DARS Numerical Simulation

A numerical simulation can help us to design DARS system. It also helps to understand and process DARS data. Previously we carried out DARS eigenvalue analysis to model its resonance frequencies. In order to simulate DARS in a more realistic way, we now use a finite difference simulator (COMSOL) to run the time harmonic modeling of DARS and apply this simulation for attenuation estimation of rock samples.

According to the exact size of experimental DARS I, we build a 3-D numerical model and perform the time harmonic analysis. The time-harmonic equation is the inhomogeneous Helmholtz equation in the frequency domain

$$\nabla \cdot \left(-\frac{1}{\rho_0} (\nabla p - q) \right) - \frac{\omega^2}{\rho_0 c_s^2} p = S$$

where $p = p(\mathbf{x}, \omega)$ is pressure and S is source. When damping exists, ρ_0 and c_s become complex quantities. In our model, a point source located at the point \mathbf{r}_0 generates a pressure wave on the cavity wall. This point source is monopole and can be described by

$$S = i\omega S_0 \delta(\mathbf{r} - \mathbf{r}_0)$$

In this numerical simulation, the key step is to choose the size of mesh grid. We use Finite-element code to generate the mesh by specifying a maximum element size of $L/6$, where $L = c/f$ is the free-space wavelength of the sound waves at the resonant frequency 1086 Hz for the empty cavity.

Attenuation is classically implemented with complex velocities. In the damping settings, we can choose frequency-independent Q or frequency-dependent Q . If we define the complex velocity by $c=c_0*(1-i*1/2Q)$, it means frequency independent Q model (Toksöz and Johnston, 1981). We can also choose dependent-frequency attenuation that is specified by the absorption coefficient $\alpha = \pi f / cQ$. Figure 6 gives an example of simulated resonance curve. The resonance frequency is the same as the lab data, but the system Q value (1646) is much higher than the lab data. We need more work to understand this problem.

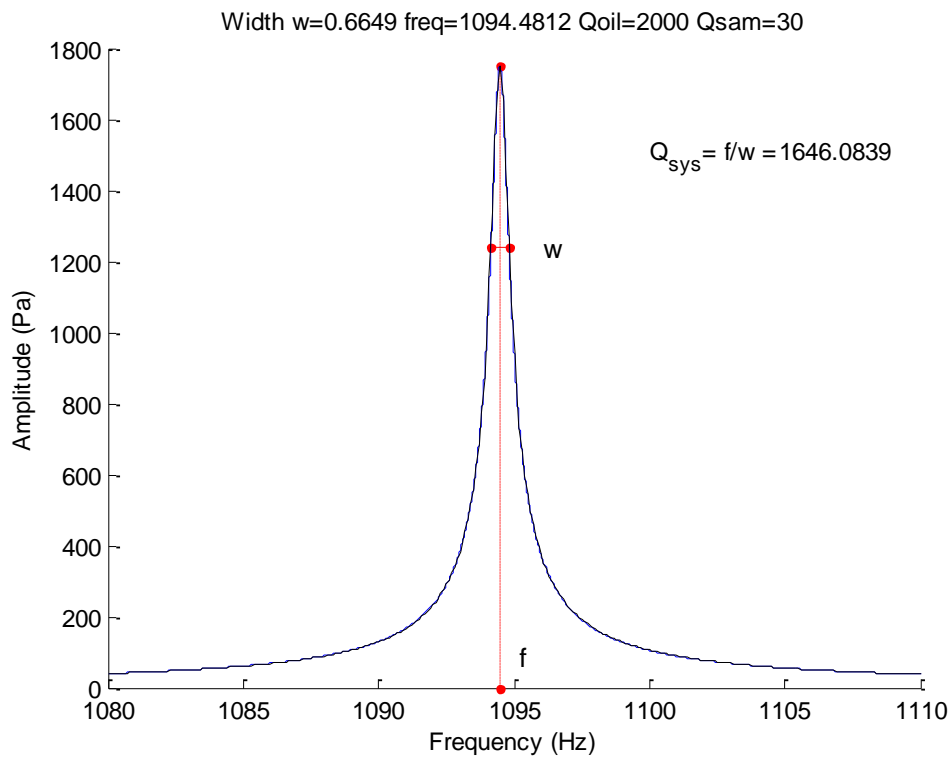


Figure 23: Simulated resonance curve. The cavity has a rock sample ($Q=30$) in it.

4. A Finite Element Algorithm for 3D Transient Electromagnetic Modeling

Seismic is probably the most powerful geophysical tool for subsurface monitoring. However, the electromagnetic (EM) method is also useful for subsurface monitoring, especially for a relatively shallow target like coalbed. The EM forward modeling is the first step for applying the EM method to surface monitoring.

We here present a 3-D finite-element time-domain (FETD) algorithm for the simulation of electromagnetic (EM) diffusion phenomena. The algorithm simulates transient electric fields and time derivatives of the magnetic fields for a general anisotropic earth. In order to compute transient fields, the electric field wave equation is transformed into a system of ordinary differential equations (ODE) via a Galerkin method with Dirichlet boundary conditions. To ensure both numerical stability and an efficient time step size, the system of ODE is discretized in time using the implicit backward Euler scheme. The resultant FETD matrix-vector equation is solved using a sparse direct solver with a fill-in reducing algorithm. When advancing the solution in time, the algorithm adjusts the time step by examining if or not a current step size can be doubled without affecting the accuracy of the solution. Instead of directly solving another FETD matrix-vector equation for transient magnetic fields, Faraday's law is employed to compute time-derivatives of magnetic fields only at receiver positions. The accuracy and efficiency of the FETD algorithm are demonstrated using time-domain controlled source EM (TD-CSEM) simulations.

Introduction

Transient electromagnetic (TEM) methods are used in both near-surface and deep exploration geophysics. Since interpretation of TEM data in complex geological environments increasingly resort to forward/inverse modeling, the numerical simulation of TEM fields is of particular interest. Among the variety of numerical simulation techniques, finite-difference time-domain (FDTD) algorithms have become the most popular for TEM simulations (Wang and Hohmann, 1993; Commer and Newman, 2004). Their popularity is due to the fact that they are relatively simple to implement, efficient, and can provide accurate solutions to a wide range of TEM simulations.

However, the FDTD method also has well known drawbacks. From a modeling point of view, its biggest weakness is that large complex geological structures (e.g. bathymetry), which do not conform to rectangular grids, need to be captured by stair-step approximations. The stair-step approximation might seem to adequately model significantly-irregular topography using a series of very small grids in parallel computing environments. However, such a stair-step modeling approach can introduce errors into numerical modeling results especially when sources and receivers are placed on the complex surface described by the fine stair steps. Furthermore, the stair-step modeling approach can introduce unnecessarily small grid spacing in the computational domain, resulting in inefficiently small time steps when the Du Fort-Frankel method is used.

We present herein a 3-D FETD algorithm as an alternative to FDTD for diffusive EM simulation in complex geological environments. In contrast to finite difference (FD) methods, finite element (FE) algorithms are based on a geometry-conforming unstructured mesh which allows precise representations of complex geological structures in computationally economic and elegant ways. The price paid is the development cost of the finite-element simulation code.

Theory and Method

In a given computational domain V , the full electric field wave equation is given as

$$\nabla \times \left[\frac{1}{\mu} \nabla \times \mathbf{e}(\mathbf{r}, t) \right] + \epsilon \frac{\partial^2 \mathbf{e}(\mathbf{r}, t)}{\partial t^2} + \sigma \frac{\partial \mathbf{e}(\mathbf{r}, t)}{\partial t} = - \frac{\partial \mathbf{j}_s(\mathbf{r}, t)}{\partial t}, \quad (8)$$

where $\mathbf{e}(\mathbf{r}, t)$ is the electric field at time t at position $\mathbf{r} \in V$, μ , ϵ , σ and $\mathbf{j}_s(\mathbf{r}, t)$ are magnetic permeability, a 3x3 dielectric permittivity tensor and a 3x3 electric conductivity tensor, and an electric current source term, respectively.

First, a residual vector for eqn. (8) is defined as

$$\begin{aligned} \mathbf{p}(\mathbf{r}, t) \equiv & \nabla \times \left[\frac{1}{\mu} \nabla \times \mathbf{e}(\mathbf{r}, t) \right] + \epsilon \frac{\partial^2 \mathbf{e}(\mathbf{r}, t)}{\partial t^2} \\ & + \sigma \frac{\partial \mathbf{e}(\mathbf{r}, t)}{\partial t} + \frac{\partial \mathbf{j}_s(\mathbf{r}, t)}{\partial t}. \end{aligned} \quad (9)$$

The residual vector must be zero everywhere within V in order to satisfy eqn. (8). However, from a numerical point of view, it is practical to discretize the computational domain into a number of finite elements. Then, the residual vector for each element is forced to be zero in a weighted-integral sense (Jin, 2002):

$$\iiint_{V^e} \mathbf{n}_i^e(\mathbf{r}) \cdot \mathbf{p}^e(\mathbf{r}, t) dV = 0 \quad (10)$$

where the superscript e denotes the e^{th} tetrahedral element, $\mathbf{n}_i^e(\mathbf{r})$ with i varying from 1 to n is a set of weighting functions, and V^e is the volume of the e^{th} tetrahedral element.

If the set of $\mathbf{n}_i^e(\mathbf{r})$ functions used in eqn. (10) is also chosen as the set of basis functions for the electric field, the electric field is expanded as

$$\mathbf{e}^e(\mathbf{r}, t) = \sum_{j=1}^n \mathbf{e}_j^e(\mathbf{r}, t) = \sum_{j=1}^n u_j^e(t) \mathbf{n}_j^e(\mathbf{r}) \quad (11)$$

where $u_j^e(t)$ is an amplitude of the electric field on the j^{th} edge of the e^{th} element and needs to be determined using the FETD method. In this study, edge-based Whitney

functions (Whitney, 1957) are chosen as the basis functions as well as weight functions for eqns. (10) and (11).

Substituting eqn. (11) into eqn. (10) and dropping the displacement current term yield the following system of 1st-order ODEs:

$$\mathbf{B}^e \frac{d\mathbf{u}^e(t)}{dt} + \mathbf{C}^e \mathbf{u}^e(t) + \mathbf{s}^e = 0 \quad (12)$$

where

$$(i,j) \text{ element of } \mathbf{B}^e = \iiint_{V^e} \mathbf{n}^e \cdot \mathbf{n}_i^e(\mathbf{r}) \cdot \mathbf{n}_j^e(\mathbf{r}) dV ; \quad (13)$$

$$(i,j) \text{ element of } \mathbf{C}^e = \iiint_{V^e} \frac{1}{\mu} \nabla \times \mathbf{n}_i^e(\mathbf{r}) \cdot \nabla \times \mathbf{n}_j^e(\mathbf{r}) dV ; \quad (14)$$

$$i \text{ element of } \mathbf{s}^e = \iiint_{V^e} \mathbf{n}_i^e(\mathbf{r}) \cdot \frac{\partial \mathbf{j}_s(\mathbf{r}, t)}{\partial t} dV ; \quad (15)$$

$$\mathbf{u}^e = [u_1^e \quad u_2^e \quad \dots \quad u_n^e] , \quad (16)$$

and n is the number of the basis functions for the e^{th} tetrahedron.

The system of ODEs is considered local because it results from each individual tetrahedral element. Using connectivity information about finite elements and applying Dirichlet boundary conditions to the boundaries of the computational domain \mathbf{V} , the local systems of diffusion equations from individual elements are assembled into a single global system of diffusion equations:

$$\mathbf{B} \frac{d\mathbf{u}(t)}{dt} + \mathbf{C} \mathbf{u}(t) + \mathbf{s} = 0 \quad (17)$$

Using an implicit 2nd-order backward Euler scheme, eqn. (17) is discretized in time into

$$\mathbf{D} \mathbf{u}^{n+2} = (3\mathbf{B} + 2\Delta t \mathbf{C}) \mathbf{u}^{n+2} = \mathbf{B} (4\mathbf{u}^{n+1} - \mathbf{u}^n) - 2\Delta t \mathbf{s}^{n+2} , \quad (18)$$

where $\mathbf{u}(t) = \mathbf{u}(n\Delta t) = \mathbf{u}^n$, and Δt is the time step size.

The most expensive part in the FE computation is advancing the solution in time. Our primary choice of the numerical solver for eqn. (18) is a direct solver. Matrix \mathbf{D} is explicitly factorized into the product of lower and upper triangular matrices \mathbf{L} and \mathbf{U} . Because Matrix \mathbf{D} is a function of Δt in eqn. (18), the factorization is performed only when Δt is changed. Before the factorization starts, matrix \mathbf{D} is re-ordered to minimize fill-in in the resulting triangular matrices. Finally, forward and backward substitution completes the solution process at a given time. When models are too large for the memory of a given computer, we use an iterative solver. In this case, the solution at the previous time step is used as the initial guess at the current time step. A preconditioner also needs to be re-constructed only when Δt is changed.

EM diffusion simulations require a very small Δt in early time to resolve the broad frequency spectrum of the induced TEM fields. However, because the high frequency component of the TEM field is more rapidly attenuated in time, one can take increasingly larger time steps and thus advance the solution quickly without affecting the accuracy. Therefore, our FETD algorithm tries to double Δt every m time steps, where m is an input parameter. If an earth model is conductive, a smaller m is chosen; if an earth model is rather resistive, a larger m needs to be chosen. When the FETD algorithm attempts to switch a time step size from Δt to $2\Delta t$, the electric fields are computed using both time steps. If the difference between the two solutions is smaller than a specified tolerance, $2\Delta t$ is accepted as a new time step. If the tolerance criterion is not satisfied, the FETD algorithm rejects $2\Delta t$ and continues using the current Δt . However, the byproduct matrices (e.g. the triangular matrices or preconditioner) for $2\Delta t$ are stored for future uses after another m time steps. For brevity, we call this approach the adaptive time step doubling method.

In order to advance eqn. (18), the initial electric fields must be provided. When an earth model is excited using a step-on or Gaussian source waveform, the initial fields are set to zero. However, when a step-off source waveform is employed, the initial DC electric fields need to be calculated via the Poisson equation. Therefore, we also solve the Poisson equation using the FE method. The FE method is based on secondary potential approach since it provides more accurate solutions near sinks and sources (Li and Spitzer, 2002). Once the electric potentials are determined at every FE node in the computational domain, the electric fields along the edges of the elements can be directly calculated using the gradients of the potentials.

After the transient electric fields are calculated in the computational domain using the FETD algorithm, the magnetic fields are determined exploiting the fact that most magnetic receivers do not measure amplitude of magnetic fields, but rather the time derivative of magnetic fields (Commer and Newman, 2004). The time derivatives can be easily determined via Faraday's law by directly applying the curl operator to the basis function in eqn. (11). In this way, we compute the time derivatives of magnetic fields only at receiver positions and avoid having to solve another matrix-vector equation for the transient magnetic field diffusion.

Time-Domain CSEM Simulation Examples

To demonstrate the accuracy and performance of our FETD algorithm, a serial implementation named FETDEM3D is written in MATLAB, from where several external routines are called. The MATLAB portion of FETDEM3D mainly includes FE pre-processing tasks, whereas the external routines are responsible for main FE computations. The FETD modeling was carried out on Sun V40z with 4 Opteron dual-core CPUs with 32 GB memory running Red Hat Linux. The results are compared with the 1D analytical or the 3D FDTD solution of Commer and Newman (2004). Although our FETD algorithm can simultaneously handle multiple arbitrarily-configured electric dipoles with various source waveforms over anisotropic media, single step-off electric dipole

responses over isotropic media are considered in this section for comparison and verification purposes.

The first example is a simple marine TD-CSEM model. The model consists of a 0.7 Ohm-m resistive homogeneous seafloor and a 400 m deep, 0.3 Ohm-m resistive seawater column. To ensure numerical stability, the resistivity of the air is set to 10,000 Ohm-m. A 250 m long, x-oriented electric dipole is placed 50 m above the seafloor. Its ramp-off time is set to $1e-2$ (seconds). Three EM receivers are placed on the seafloor at $x=2, 4$ and 6 km source-receiver offsets. The model is discretized into 108,540 tetrahedral elements, generating 125,883 unknowns. The FETD solutions are plotted in Figure 24, showing excellent agreement with the analytical solutions.

Figure 25 summarizes the performance of the adaptive time step doubling method for the seafloor model above. Without the method, it took 16.2 hours with 50,000 time steps to complete the simulation. In contrast, when the doubling method was employed, the simulation was completed in 36 minutes with 1,393 time-steps. The time step doubling procedures were performed 8 times.

The next example is a 3-D resistive gas reservoir model shown in Figure 26a. The inline TD-CSEM responses over the gas reservoir are simulated using both 3-D FDTD and FETD algorithms. A 250 m long electric dipole whose ramp-off time is set to $1E-4$ seconds is placed at the center of the model. The 3-D FDTD solutions for the model were imported from Um (2005). The FETD algorithm discretizes the model into 114,116 tetrahedral elements, generating 131,741 unknowns. It took 53 minutes to complete the FETD simulation with a total of 1,559 time steps when the adaptive time step doubling method is employed. The solutions from both the FETD and FDTD methods are plotted together in Figures 26b and 26c. The curves for each receiver position agree well with each other at most times except at very early times where slight differences in the electric fields are observed because the employed FD grid does not handle high frequency EM signals very well.

The final example is a gently dipping (4 degrees) two-dimensional (2D) seafloor with and without a 3-D hydrocarbon reservoir illustrated in Figure 27a. In order to elucidate the effects of the slope on the marine TD-CSEM method, a flat seafloor model with and without the same hydrocarbon reservoir is also simulated. The flat seafloor model has a uniform 400 m thick seawater column. The dipping and flat seafloor models are discretized into 165,528 tetrahedral elements with 191,780 unknowns and 127,046 tetrahedral elements with 146,871 unknowns, respectively. The simulations were completed in 65 and 41 minutes, respectively. The inline electric field responses at 4 km source-receiver offset are plotted in Figures 27b and 27c. The differences observed in Figure 27 can be thought of as the combination of the following factors: 1) the airwave effect varies as the thickness of the seawater column above the receiver changes due to the bathymetry; 2) the receiver coordinate is tilted towards the slope; 3) the receiver on the slope measures stronger galvanic effects than that on the flat seafloor because of its shorter distance from the hydrocarbon reservoir. In short, a gently-dipping simple seafloor structure can cause significant effects on the TD-CSEM measurements and, as demonstrated above, seafloor bathymetry needs to be modeled with special care.

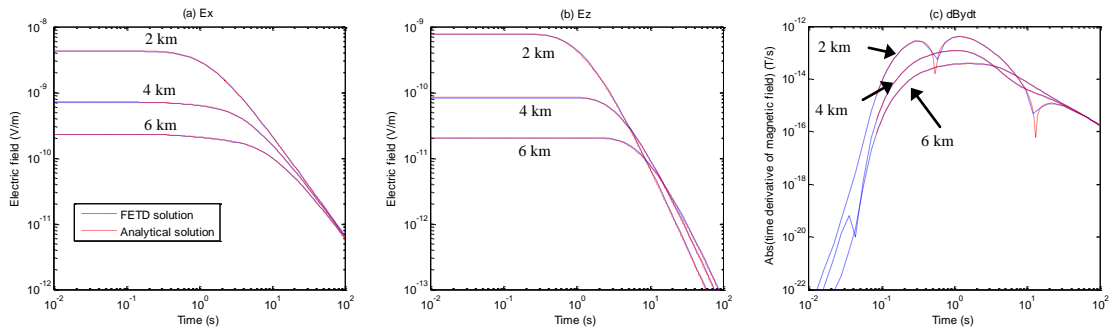


Figure 24: In-line TD-CSEM responses at 2, 4 and 6 km source-receiver offsets over the homogeneous seafloor model.

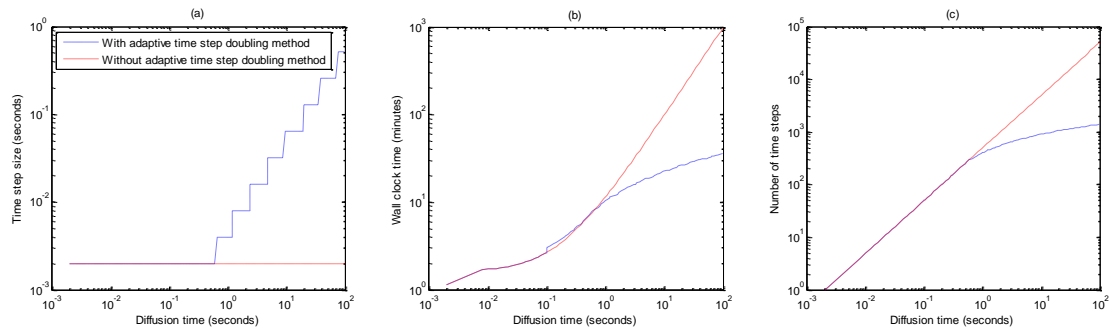


Figure 25: Comparison of computational efficiency with and without the time step doubling method.

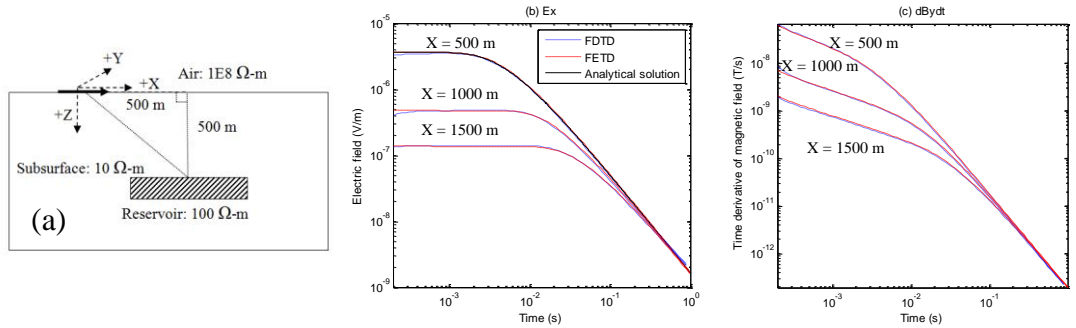


Figure 26. (a) The 3-D gas reservoir model. (b) Ex fields from FETD and FDTD. (c) dBydt fields from FETD and FDTD.

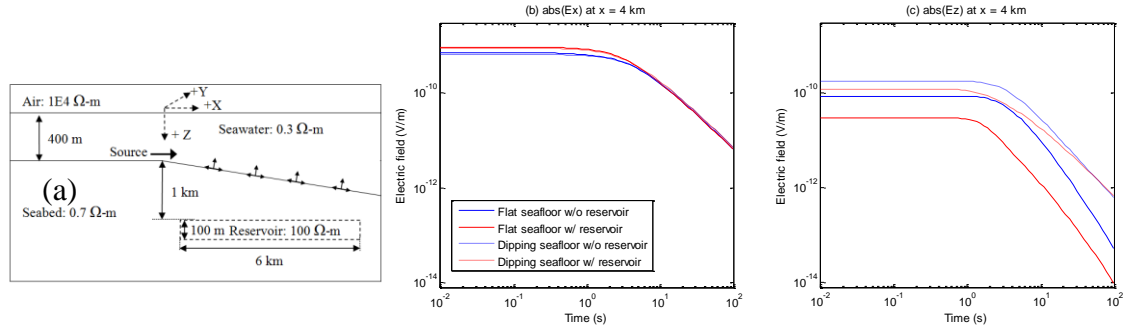


Figure 27. (a) The 2D seafloor model with and without the 3D reservoir. (b) Ex fields. (c) Ez fields. The size of the 3D reservoir is 6 (km)-by-6 (km)-by 0.1 (km) in the x-, y- and z- directions, respectively. Its axis base point is (1 km, -3 m, 1500 m).

Summary – Electromagnetic Simulations

We have presented an efficient 3-D FETD algorithm to simulate diffusive electromagnetic phenomena. The algorithm is especially useful for modeling complex topography and reservoir geometry. The FETD algorithm uses an implicit backward Euler scheme to retain numerical stability with a larger time step size that helps accelerate FETD solution processes especially in late time. The inherent high-computational efforts associated with solving the resultant FETD matrix-vector equation at every time step are mitigated by re-factorizing the FETD matrix only when a time step size is changed. By adaptively doubling the time step at intervals, the FETD algorithm trades off the computational cost of re-factorizing the FETD matrix for the faster advance in FETD solutions. The adaptive time step doubling method plays an important role in speeding up the FETD computation especially in a marine TD-CSEM simulation where an EM diffusion process occurs slowly until very late time due to the high electrical conductivities.

Future Work

True 4-D is a new concept for seismic subsurface monitoring. There are many researches must be done before applying it for real world. We will run more examples for embedded acquisition system using the finite difference method and apply the dynamic inversion to the simulated pre-stack data. For the data evolution work, we will apply our method to surface reflection data. We also plan to use the EM modeling algorithm to run surface and borehole monitoring scenarios.

Publications

Arogunmati, A. and J. M. Harris, 2009, An approach for quasi-continuous time-lapse seismic monitoring with sparse data: Expanded Abstract submitted to the 2009 Annual Meeting, Houston.

Um, E. and J. M. Harris, 2009, A finite element algorithm for 3D transient electromagnetic modeling: Expanded Abstract submitted to the 2009 Annual Meeting, Houston.

References

Arts, R., Eiken, O., Chadwick, A., Zweigel, P., van der Meer, L., Zinszner, B., 2004, Monitoring of CO₂ injected at Sleipner using time-lapse seismic data: *Energy*, **29**, 1383–1392.

Candès, E., and Romberg, J., 2007, Sparsity and incoherence in compressive sampling: *Inverse Problems* **23**, 969–985

Commer, M., and G. Newman, 2004, A parallel finite-difference approach for 3D transient electromagnetic modeling with galvanic sources: *Geophysics*, **69**, 1192-1202.

Harris, J. M., Y. Quan, C. Xu, and J. Urban, 2006, Seismic Monitoring of CO₂ Sequestration: GCEP Annual Report.

Harris, J. M., Nolen-Hoeksema, R. C., Langan, R. T., Van Schaack, M., Lazaratos, S. K., Rector III, J. W., 1995, High resolution crosswell imaging of a west Texas carbonate reservoir: Part 1-Project summary and interpretation: *Geophysics*, **60**, 667-681.

Harris, J. M., Zoback, M. D., Kovscek, A. R., Orr, F. M. Jr, 2004, Geologic Storage of CO₂, in *Global Climate and Energy Project 2008 Technical Report*, section 2.5.3.

Harris, J. M., Zoback, M. D., Kovscek, A. R., Orr, F. M. Jr, 2007, Geologic Storage of CO₂, in *Global Climate and Energy Project 2008 Technical Report*, section 2.5.3.

Harris, J. M., Zoback, M. D., Kavscek, A. R., Orr, F. M. Jr, 2008, Geologic Storage of CO₂, in Global Climate and Energy Project 2008 Technical Report, section 2.5.3.

Hole, J. A., and Zelt, B. C., 1995, 3-D finite-difference reflection traveltimes: *Geophysical Journal International*, **121**, 427-43

Lazaratos, S. K., and Marion, B. P., 1997, Crosswell seismic imaging of reservoir changes caused by CO₂ injection: *The Leading Edge*, **16**, 1300-1306.

Landrø M., Solheim, O. A., Hilde, E., Ekren, B. O., Strønen, L. K., 1999, The Gullfaks 4D seismic study: [Petroleum Geoscience](#), **5**, 213-226.

Lecomte, I., and T. Kaschwich, 2008, Closer to real earth in reservoir characterization: a 3D isotropic/anisotropic PSDM simulator: *SEG Expanded Abstracts*.

Li, Y. and K. Spitzer, 2002, Three-dimensional DC resistivity forward modeling using finite elements in comparison with finite-difference solutions: *Geophysical Journal International*, **151**, 924-934.

Mathisen, M. E., Vasiliou, A. A., Cunningham, P., Shaw, J., Justice, J. H., Guinzy, N. J., 1995, Time-lapse crosswell seismic tomogram interpretation: Implications for heavy oil reservoir characterization, thermal recovery process monitoring, and tomographic imaging technology: *Geophysics*, **60**, 631-650.

Jin, J., 2002, *The finite element method in electromagnetics*, 2nd edition: John Wiley and Sons.

Jin, L., M.K. Sen, and P.L. Stoffa, 2008, One-dimensional prestack seismic waveform inversion Using Ensemble Kalman Filter: *SEG Expanded Abstracts*.

Quan, Y. and J.M. Harris, 2008, Stochastic Seismic Inversion using both Waveform and Traveltime Data and Its Application to Time-lapse Monitoring: *SEG Expanded Abstracts*.

Rickett, J. E., and Lumley, D. E., 2001, Cross-equalization data processing for time-lapse seismic reservoir monitoring: A case study from the Gulf of Mexico: *Geophysics*, **66**, 1015–1025.

Ross, H. E, 2007, Carbon dioxide sequestration and enhanced coalbed methane recovery in unmineable coalbeds of the powder river basin, Wyoming: PhD Thesis, Stanford University.

Toksöz and Johnston, 1981, Seismic wave attenuation: *SEG Expanded Abstracts*

Um, E. S., 2005, On the physics of galvanic source electromagnetic

geophysical methods for terrestrial and marine exploration: M.S. thesis, University of Wisconsin-Madison.

Walton, G. G, 1972, Three-dimensional seismic method: *Geophysics*, 37, 417–430.

Wang, T., and G. W. Hohmann, 1993, A finite-difference, time-domain solution for three-dimensional electromagnetic modeling: *Geophysics*, 58, 797-809.

Whitney, H., 1957, *Geometric integration theory*: Princeton University Press.

Wynn, D., 2003, Survey of geophysical monitoring methods for monitoring CO2 sequestration in aquifers. M.S. Thesis, Department of Geophysics, Stanford University.

Yilmaz, O., 1987, *Seismic Data Processing*, S. M. Doherty: Society of Exploration Geophysicists, Tulsa.

Yilmaz, O., 2001, *Seismic Data Analysis: Processing, Inversion, and Interpretation of Seismic*: Society of Exploration Geophysicists, Tulsa.

Zelt, C. A., and Barton, P. J., 1998, 3D seismic refraction tomography: A comparison of two methods applied to data from the Faeroe Basin: *JGR*, **103**, 7187-7210.

Acknowledgements

The authors JMH, YQ, JR-M and YA are grateful to GCEP for support of their work on this project. TZ and EU thank the SGFs and the SES for their fellowship support.

Contacts

Jerry M. Harris: jerry.harris@stanford.edu

Youli Quan: quany@stanford.edu

Adeyemi Arogunmati: aadeyemi@stanford.edu

Jolene Robin-McCaskill: jmrobin@stanford.edu

Evan Um: eum@stanford.edu

Tieyuan Zhu: tyzhu@stanford.edu